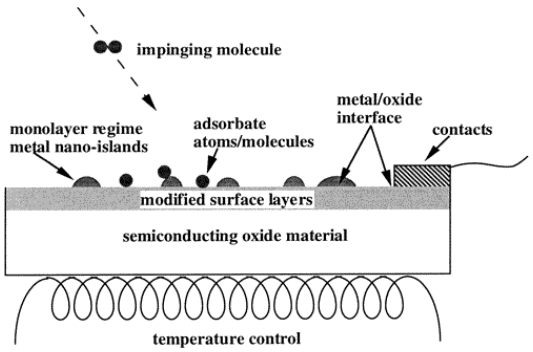

Figure 1: Generalized schematic of a planar gas sensing interface.

"Kinetically controlled chemical sensing using micromachined structures," Steve Semancik and Richard Cavicchi, Acc. Chem. Res. **1998** *31*, 279-287.

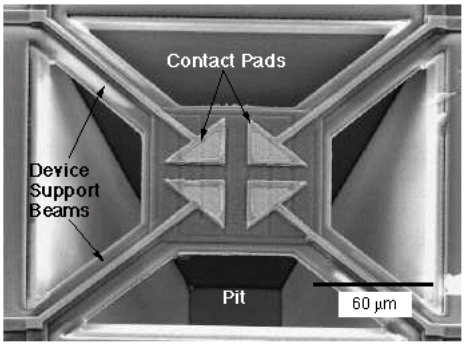

Figure 2: Micrograph of a single micro-hotplate.

"Kinetically controlled chemical sensing using micromachined structures," Steve Semancik and Richard Cavicchi, Acc. Chem. Res. **1998** *31*, 279-287.

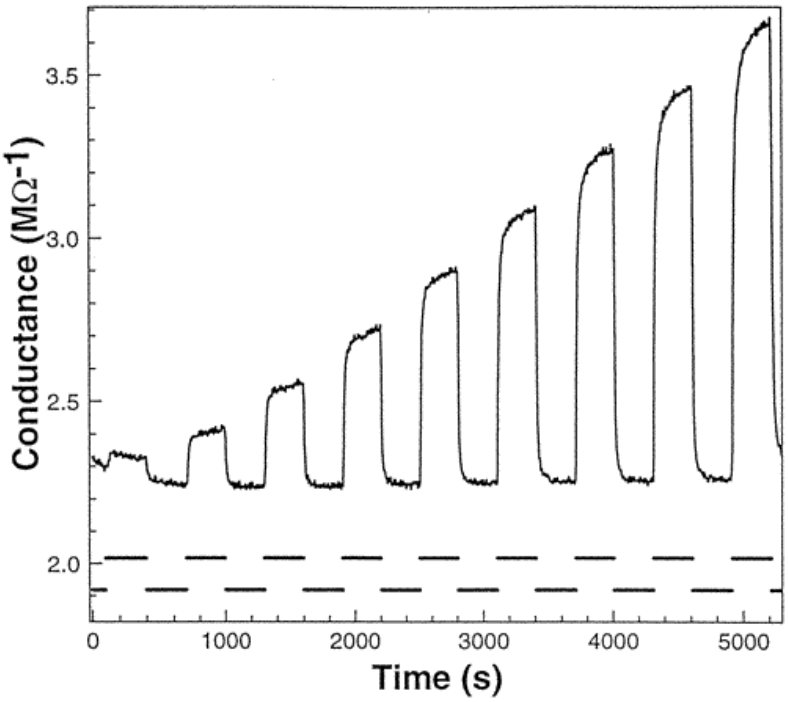

Figure 3: Static mode response at 130 C of a Pt/SnO_2 microsensor to on/off CO exposures, into (dry) air, of increasing concentrations from 5 to 45 ppm.

"Kinetically controlled chemical sensing using micromachined structures," Steve Semancik and Richard Cavicchi, Acc. Chem. Res. **1998** *31*, 279-287.

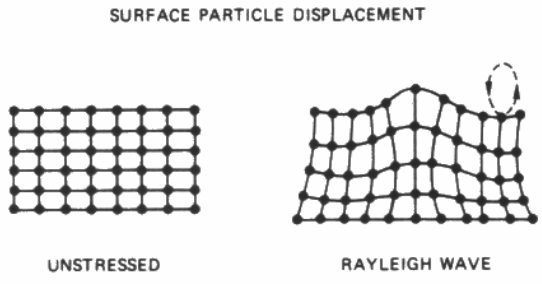

Figure 4: Deformation of the SAW substrate resulting from the propagation of a Rayleigh surface wave. The vertical displacement amplitude is typically about 10 A.

"Mechanism of operation and design considerations for surface acoustic wave device vapour sensors," Hank Wohltjen, Sensors and Actuators **5** (1984) 307-325.

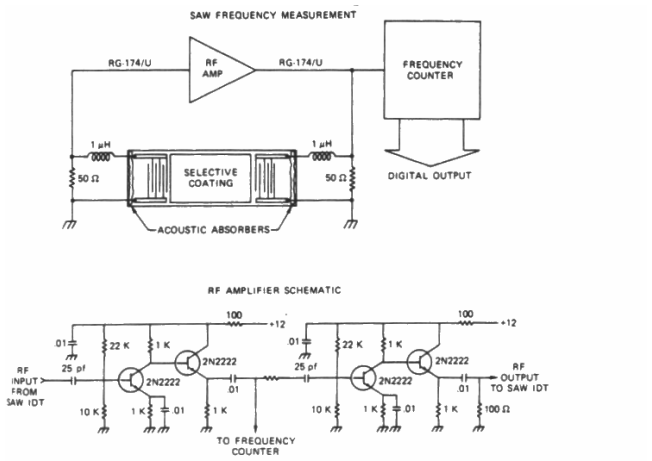

Figure 5: SAW delay line oscillator system (top) and RF amplifier schematic (bottom).

"Mechanism of operation and design considerations for surface acoustic wave device vapour sensors," Hank Wohltjen, Sensors and Actuators **5** (1984) 307-325.

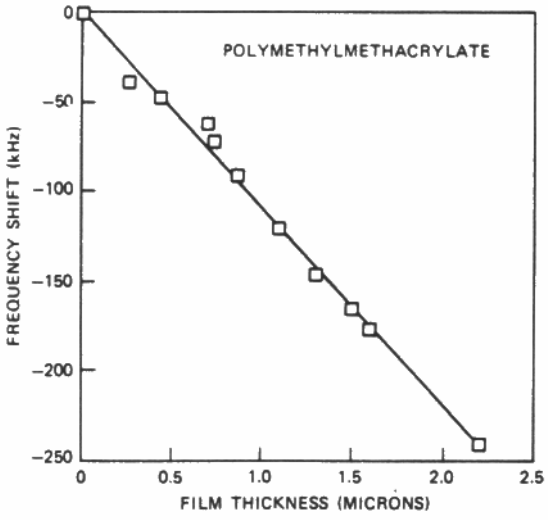

Figure 6: SAW oscillator frequency shift produced by various thicknesses of poly(methylmethacrylate).

"Mechanism of operation and design considerations for surface acoustic wave device vapour sensors," Hank Wohltjen, Sensors and Actuators **5** (1984) 307-325.

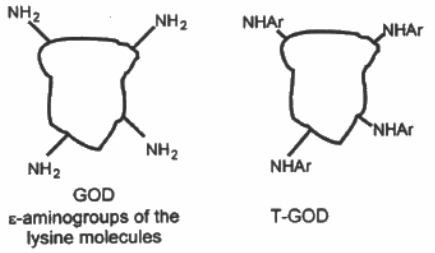

Figure 7:

"Immunosensing of photoimmobilized proteins on surface acoustic wave sensors," Thomas Wessa, Michael Rapp and Hans Sigrist, Colloids and Surfaces B: Biointerfaces **15** (1999) 139-146.

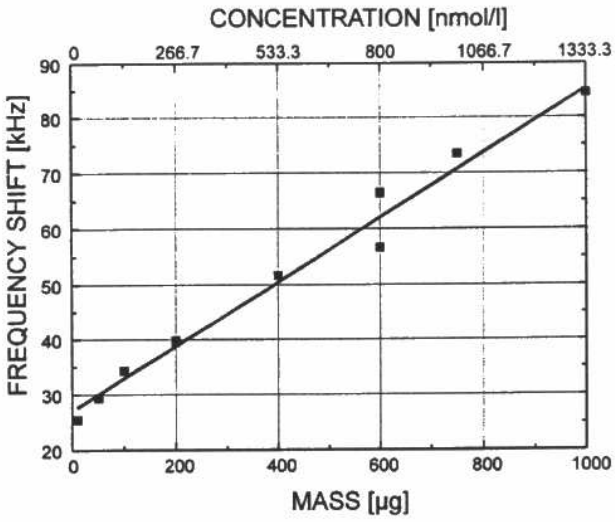

Figure 8: Change of resonance frequency as a function of the analyte concentration. SAW sensors were coated with T-GOD and probed with polyclonal anti-GOD antibodies.

"Immunosensing of photoimmobilized proteins on surface acoustic wave sensors," Thomas Wessa, Michael Rapp and Hans Sigrist, Colloids and Surfaces B: Biointerfaces **15** (1999) 139-146.

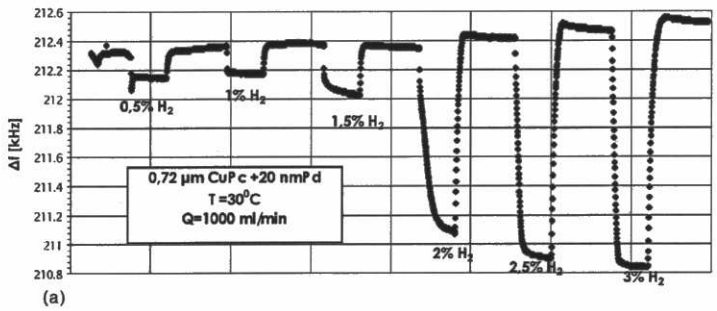

Figure 9: Changes in the differential frequency Δf vs. time for a bilayer sensor structure at 30 C and six different concentrations of hydrogen in nitrogen (0.5 to 3%).

"Bilayer structure for hydrogen detection in a surface acoustic wave sensor system," Wieslaw P. Jakubik et al., Sensors and Actuators **82** (2002) 265-271.

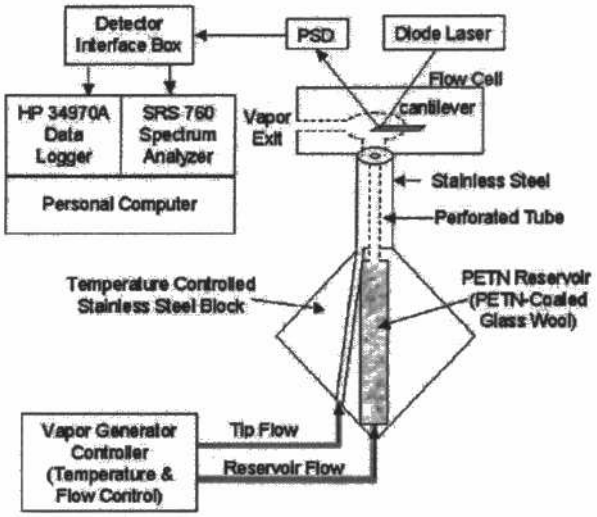

Figure 10: Schematic diagram of the experimental apparatus showing the PETN vapor generator. A similar generator was used for RDX measurements.

"Sensitive detection of plastic explosives with self-assembled monolayer-coated microcantilevers," L. A. Pinnaduwage et al., Applied Physics Letters **83** (2003) 1471-1473.

Figure 11: When explosive compounds bind to these V-shaped cantilevers, the microscopic structures bend and produce a signal.

"Bomb Sniffer," Science News **164** (2003) 116.

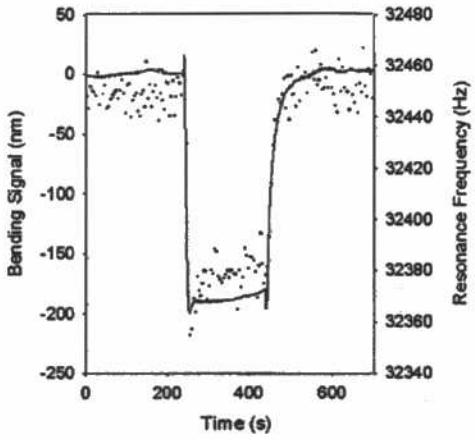

Figure 12: The response of a 4-MBA-coated silicon cantilever to a PETN stream of 1.4 ppb concentration in ambient air. The solid curve depicts the bending response, and the dots depcit the resonance frequency of the cantilever. The frequency shift due to the adsorption of PETN vapor corresponds to a mass loading of 15 pg on the cantilever.

"Sensitive detection of plastic explosives with self-assembled monolayer-coated microcantilevers," L. A. Pinnaduwage et al., Applied Physics Letters **83** (2003) 1471-1473.